CRYSTAL GROWTH & DESIGN

pubs.acs.org/crystal

Article

Synthesis and Adsorbent Properties of Silica-Titanate Nanoarchitectures Produced by Unrolling Titanate Tubular Sheets

Published as part of a Crystal Growth and Design virtual special issue on Zeolite Crystal Engineering

Anderson J. Schwanke,* Wesley Monteiro, Letícia G. da Trindade, Elson Longo, Katia Bernardo-Gusmão, and Michèle O. de Souza*

Cite This: *Cryst. Growth Des.* 2023, 23, 1925−1934

Read Online

ACCESS | Metrics & More | Article Recommendations

ABSTRACT: Microporous and mesoporous nanocomposites based on silica and titanate are obtained by unrolling sodic titanate nanotubes. The opened titanate sheets are then spaced by introducing surfactant species via ion exchange and introducing silica species between the unrolled titanate nanotubes. The characterization indicates an organic−inorganic hybrid intermediate resulting from the surfactant in perpendicular accommodation between the open tubular sheets. Stabilizing the silica spacers resulted in a microporous and mesoporous nanoarchitecture forming voids between the unrolled titanate sheets with a higher specific surface (714 m^2 g^{-1}) than that of the pristine titanate nanotube (58 m^2 g^{-1}). The adsorptive properties of the synthesized silica−titanate nanoarchitectures are reported using Methylene Blue (MB) and Rhodamine B (RhB) dyes. It was revealed that the adsorption capacity against RhB is substantially increased for the nanocomposite (65%), compared to titanate nanotubes (13%). The kinetic analysis suggests that the pseudo-second-order kinetic model best describes the adsorption dynamics. Freundlich adsorption isotherm best fits the adsorption data, which suggests that adsorption does not occur onto uniform sites but in multilayers onto nanocomposites.

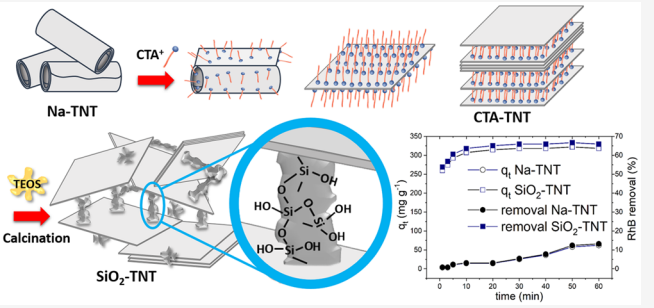

1. INTRODUCTION

In the last few decades, much effort has been put forth in obtaining titanium-based nanostructured materials[1] as these materials would have applications in several different areas, including adsorption, ion exchange, catalysis, energy, and biomedicine.[2] Titanium-based materials can be classified into two classes of structures: the polymorph titania-based structures [rutile, anatase, brookite, and a more exotic phase of pure titania, TiO_2(B)] and those formally called lamellar titanates.[3] Both classes are structurally similar, since they are formed by octahedral TiO_6 units sharing corners and edges. However, lamellar titanates are notable due to their unique characteristics, such as a more open crystal structure and a high density of negative charge compensated by cations located between the titanate sheets.[4] These lamellar materials can be formed primarily by sheet stacking described as titanate bulks or by an assembly of nanotubes whose walls are formed by a sheet rolled up on itself.

Bulk lamellar titanate were the first to be synthesized using solid-state methodologies. These two-dimensional (2D) materials were obtained by mixing titanium oxide and carbonates of the desired charge-compensating metals, e.g., Na, K,[5] Cs,[6] under high temperatures (~800−1000 °C) and synthesis times (1−3 days). Bulk lamellar titanate in proton form is obtained when the original compensation cations are exchanged with protons through successive exchanges using fresh solutions of HCl or HNO_3. However, bulk lamellar titanates have large particle sizes with low specific surface area, limiting their application.[3]

One way to increase the accessibility to the internal porosity of bulk lamellar titanates and their specific surface area is through the process of pillaring and exfoliation. However, the intercalation of positively charged organic species between the titanate sheets must be performed before applying these processes. These organic molecules, such as neutral amines of different sizes, through interaction with the protonated titanates via NH_4^+ bonds, act as spacer agents of the lamellae, thereby increasing the distance between them. The pillaring

Received: December 11, 2022
Revised: February 3, 2023
Published: February 14, 2023

https://doi.org/10.1021/acs.cgd.2c01471
Cryst. Growth Des. 2023, 23, 1925−1934

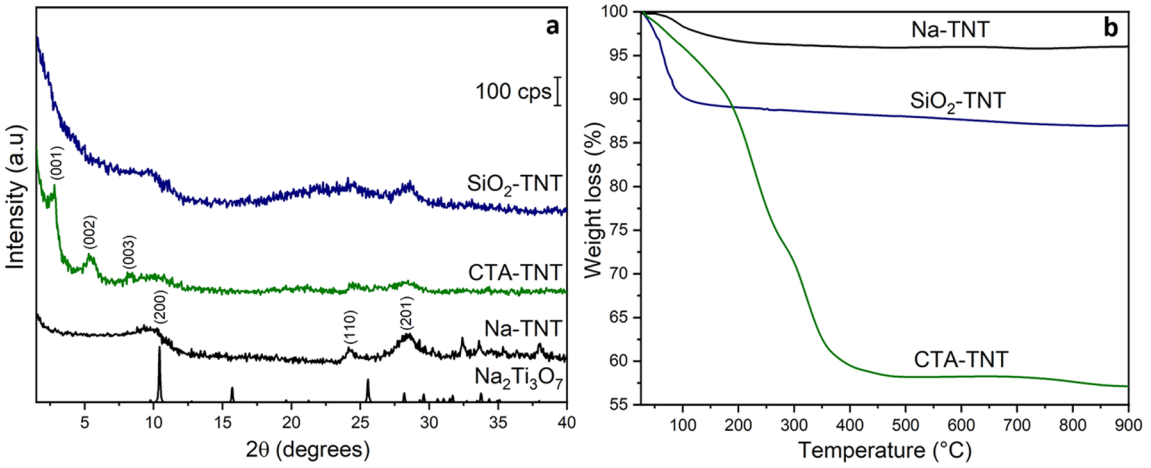

Figure 1. (a) XRD patterns and (b) TGA curves of Na-TNT, CTA-TNT, and SiO_2-TNT samples. The $Na_2Ti_3O_7$ was used as a reference.

procedure consists of adding a pillaring precursor that fills the spaces previously formed between the lamellae with elements that will form 2D heterostructures, including silicon,[7] aluminum,[8,9] or titanium oxides,[10,11] between the lamellae after the calcination of the material. Exfoliation is performed by treating bulk lamellar titanates with organic molecules under sonication, resulting in the loss of the lamellar stacking order in the titanate sheets and the formation of a more-open three-dimensional (3D) structure after calcination.[12]

In 1998, Kasuga et al. reported the synthesis of one-dimensional (1D) titanate nanotubes performed under hydrothermal conditions using TiO_2, alkaline solution (10 mol L^{-1} of NaOH), and temperatures between 100 °C and 150 °C.[13] These conditions are friendly, compared to the bulk lamellar titanate, because high temperatures are not required to obtain the complete conversion of titanium precursors into nanotubes. Although the tubular formation mechanism is not fully understood, it has been suggested that the sheet curling occurs due to mechanical stress forces during dissolution and crystallization.[14] The periodicity of the rolled titanate sheets results in the formation of multi walls, detected through X-ray diffraction analysis of the titanate nanotube samples in the presence of a large peak at 2θ = 10.2°, corresponding to an interplanar distance of 0.86 nm. The nanotubes presented lengths between 50 and 100 nm, and the rolling of the titanate sheets generated 1D channels with internal and external diameters of 4−8 nm and 8−15 nm, respectively.[4] Because of their physical and chemical properties, these materials attain properties with diverse applications, such as adsorbents,[15] ion exchangers,[16] catalysts,[17] flame retardants,[18] battery electrodes,[19] antibacterial materials,[20] and anticancer materials.[21]

In 2008, Gao et al. reported the synthesis of 2D titanate nanosheets by unrolling 1D titanate nanotubes through an ion exchange procedure.[22] Similar to bulk lamellar titanates, nanotubes are protonated through ion exchange in acidic HNO_3 solutions, followed by treatment with a tetrabutylammonium hydroxide (TBAOH) solution to increase the spacing between the sheets. The effect of TBAOH as a spacer agent that induces the nanotubes to unwind was confirmed by the presence of basal reflections in the XRD pattern with an interplanar distance of 1.88 nm, which corresponds to the sum of the size of the TBA^+ intercalated ions (0.95−1.05 nm) and the thickness of the titanate sheet (0.86 nm).

To the best of our knowledge, the intercalation of organic molecules into lamellar titanates had always been performed with protonated titanates. No studies exploring alternative methodologies have been performed to date. This work presents a new methodology for obtaining silica−titanate nanoarchitectures. Sodium titanate nanotubes are opened with cationic surfactants, and then silica spacers are introduced between the unrolled titanate layers. The synthesis of these silica−titanate nanoarchitectures produced by unrolling titanate tubular sheets, their characterization, and their adsorptive properties are reported.

2. EXPERIMENTAL SECTION

2.1. Synthesis of Sodic Titanate Nanotubes (Na-TNT). Sodic titanate nanotubes (Na-TNT) were synthesized according to the literature.[23] In a beaker, 1.5 g of TiO_2 (SB Química, anatase, 95%) was added to 120 mL of a sodium hydroxide (NaOH, Sigma−Aldrich, 98%) solution (10 mol L^{-1}) at 25 °C for 1 h with stirring. The solution was transferred into a stainless-steel autoclave with PFTE internal coating and maintained at 135 °C for 72 h. The solid was separated via centrifuge, washed with water until reaching pH 8, and dried at 85 °C for 6 h.

2.2. Synthesis of Silica-Titanate Nanoarchitectures (SiO_2-TNT). In a beaker, 3.0 g of Na-TNT were added to 90 mL of water and stirred for 1 h. Afterward, 10.5 mL of a solution of 0.44 mol L^{-1} of cetiltrimethylammonium bromide (CTAB, Sigma−Aldrich, 98%) was added and kept under stirring at 25 °C for 1 day. Then, the solid was filtered and washed thoroughly with deionized water. The $AgNO_3$ test was used until the presence of surfactant in the washing water was no longer observed. The solid was dried in an oven at 80 °C for 1 day, and the organic−inorganic hybrid intermediate was named CTA-TNT. The resulting solid was added to 0.75 g of melted dodecylamine and stirred for 4 h. The solid was added to 10.5 g of TEOS and stirred for 1 h. The material was then calcined at 600 °C for 5 h with a heating rate of 0.03 °C s^{-1}, leading to a material named SiO_2-TNT.

2.3. Adsorption Tests. Two representative dyes, Methylene Blue (MB) and Rhodamine B (RhB), dissolved in water (1×10^{-3} mol L^{-1}), were used to measure the capacity of dye adsorption of the Na-TNT and SiO_2-TNT samples. In addition, several experiments were conducted to understand the adsorption dynamics of these particles in RhB as they showed a distinct adsorption behavior, relative to that in the MB dye. Various parameters such as adsorbent dose (0.01−0.06 g), adsorbate (RhB dye) concentration (120−480 mg L^{-1}), and interval time were optimized. For these tests, known amounts of adsorbent were agitated at 150 rpm with 50 mL of the aqueous dye solution at 25 °C. After that, the resulting solution was centrifuged, and the supernatant was analyzed with an ultraviolet−visible light

https://doi.org/10.1021/acs.cgd.2c01471
Cryst. Growth Des. 2023, 23, 1925−1934

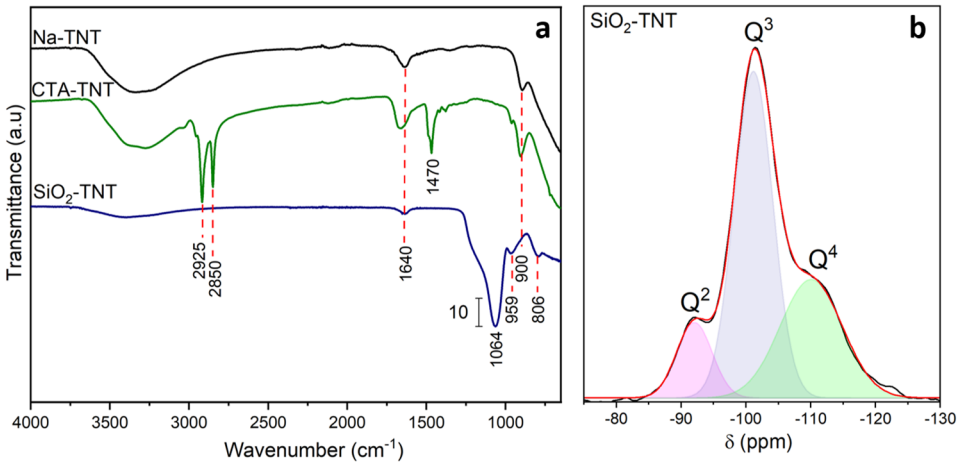

Figure 2. FTIR spectra of (a) Na-TNT, CTA-TNT, and SiO_2-TNT samples and (b) ^{29}Si CP/MAS NMR of the SiO_2-TNT sample.

(UV-vis) spectrophotometer (Model V-660, Jasco) to estimate the dye concentration at a maximum absorption wavelength of 554 nm.

The quantity of RhB adsorbed on Na-TNT, or SiO_2-TNT particles, was calculated by eq 1, and the percentage removal (%R) was calculated by eq 2:

$$q_t = \left(\frac{C_i - C_f}{m}\right) \times V \quad (1)$$

$$\%R = \left(\frac{C_i - C_t}{C_t}\right) \times 100 \quad (2)$$

where C_i is the initial RhB concentration (g L^{-1}), C_f the final RhB concentration (g L^{-1}), C_t the RhB concentration at time t (g L^{-1}), V the volume of the dye solution (L), and m the mass of the tested adsorbent (g).

2.4. Characterization. The crystalline structure of the solids was determined by X-ray diffractometry (XRD) on a Rigaku Ultima IV, using Cu Kα_1 (λ = 1.54056 Å) radiation. Fourier-transform infrared spectroscopy (FTIR) scans were performed using an ATR accessory on a Bruker Alpha II system. Thermogravimetric (TG) analyses were performed on a TA Instruments Model SDT Q600 system under flowing N_2. Atomic absorption spectroscopy (AAS) analysis was performed on a PerkinElmer Model AAnalyst 200 system with the samples previously digested in concentrated HF and HNO_3. The ^{29}Si nuclear magnetic resonance with cross-polarization (CP/MAS NMR) was performed in an Agilent 500 MHz DD2 system. Transmission electron microscopy (TEM) images were obtained using a 200 kV Tecnai Model G2 T20 system. The porosity was determined by N_2 sorption at −196 °C using a Micromeritics TriStar II 3020 system. The surface area (S_{BET}) and micropore volume (V_{micro}) were estimated by using the BET and t-plot equations, respectively. The pore size distribution (PSD) was determined using the nonlocal density functional theory (NLDFT) method for pillared clays.[24] UV-vis diffuse reflectance spectra were obtained using a Cary 5G (Varian) spectrophotometer and converted to absorption spectra according to the Tauc Plot equation.

3. RESULTS AND DISCUSSION

The diffractograms of Na-TNT, CTA-TNT, and SiO_2-TNT samples are shown in Figure 1a. The Na-TNT diffractogram exhibits three broad main peaks at 2θ = 10°, 24°, and 28°, which correspond to the crystallographic planes (200), (110), and (211), respectively. The peak at 2θ = 10° is related to a d-spacing of 0.86 nm.[21,25] Those peaks are consistent with the crystallographic information for the $Na_2Ti_3O_7{\cdot}nH_2O$ phase (JCPDS File No. 13-3129). Moreover, TiO_2 phases are absent from this diffractogram.

The XRD pattern of CTA-TNT material, after the ion exchange with surfactant, reveals a new peak at a low angle (2θ = 2.8°) attributed to the (001) layer reflection. Moreover, the peaks at 2θ = 5.4° and 8.2°, assigned as the (002) and (003) reflections, respectively, indicate a layer structure with long-range ordering. This result indicates that the exchanged CTA surfactant allowed the tubular titanates to be unrolled and to assemble flat multilayers into a high order of lamellar stacking. Therefore, the loss of the tubular structure is a consequence of the formation of the lamellar (2D) structure. The increased d-spacing of 3.20 nm, compared to the 0.86 nm of the pristine Na-TNT sample, reveals that CTA molecules effectively separated the titanate multilayers with a height of 2.34 nm. Since the theoretical length of the CTA molecule is ∼2.0 nm,[26] this result indicates that the CTA molecules adopted a perpendicular accommodation between lamellae. However, the remaining peak at 2θ = 10° could indicate some partially unrolled titanate layers that were not separated by the CTA molecules (without increasing the d-spacing) or some nanotubes that remain wrapped. The XRD pattern of SiO_2-TNT reveals the presence of a broadband reflection at low 2θ angles. The lack of (001), (002), and (003) reflections reveals that the introduction of TEOS and the subsequent calcination cause a loss of stacking order of the titanate layers and indicate a delamination phenomenon. Moreover, the broadening of the background region at 2θ = 15°−30° confirms the presence of amorphous silica in the final material.

The TGA analysis in Figure 1b confirms the presence of surfactant molecules in CTA-TNT material. As expected, a higher total weight loss (43%) occurred for the CTA-TNT sample, with the highest loss (33%) occurring between 180 and 420 °C, corresponding to the surfactant decomposition. That loss is divided into two events. The first event occurs between 180 °C and 290 °C (loss of 18%) and corresponds to the elimination of surfactant in a weak interaction with the titanate sheets. A shoulder indicates the second event at a higher temperature, between 290 °C and 420 °C (loss of 15%), related to the elimination of surfactant strongly interacting with the titanate sheets. Finally, the SiO_2-TNT showed a total weight loss of 13%, where the main loss occurred between 25 °C and 120 °C and relates to the elimination of water physically adsorbed. The total weight loss of the Na-TNT sample was 4%, corresponding to the elimination of water physically adsorbed (between 25 °C and 100 °C) and OH

https://doi.org/10.1021/acs.cgd.2c01471
Cryst. Growth Des. 2023, 23, 1925−1934

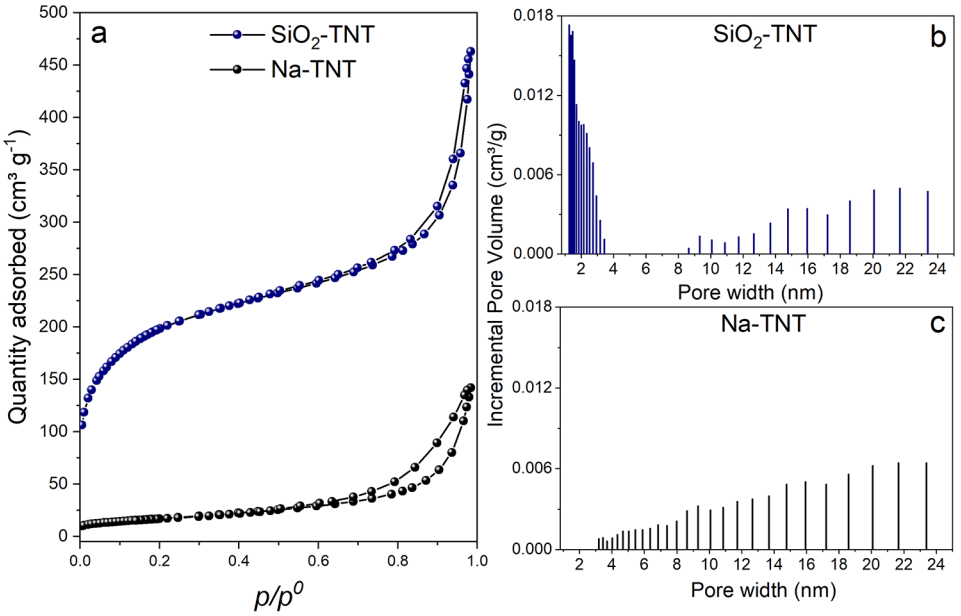

Figure 3. (a) N_2 adsorption/desorption isotherms of Na-TNT and SiO_2-TNT samples. (b, c) Pore size distribution of the SiO_2-TNT sample (panel (b)) and the Na-TNT sample (panel (c)).

groups present at the TNT surface (between 100 °C and 200 °C), which is typical of sodic titanate nanotubes.[27]

The FTIR analyses of Na-TNT, CTA-TNT, and SiO_2-TNT materials are presented in Figure 2a. All spectra present broad bands in the range of 3400−3300 and 1640 cm^{-1}, which are characteristic of the OH groups' axial and angular deformation, respectively. The Na-TNT spectrum exhibits bands at 900 cm^{-1} assigned to the Ti−O stretching vibration of a four-coordinated Ti−O structure.[28] The three signals, characteristic of the surfactant molecules, are clearly observed in the CTA-TNT spectrum. The bands at 2925 and 2850 cm^{-1} correspond to the asymmetrical and symmetrical stretching vibrations of CH_2 bonds, respectively. The band at 1470 cm^{-1} correlates to the symmetrical bending vibrations of C−H bonds.[29]

The SiO_2-TNT spectrum reveals that, after the TEOS introduction and calcination, the surfactant molecules were entirely removed, and a new broadband emerged at 1064 cm^{-1}, corresponding to the asymmetric vibrations of Si−O−Si bonds. Moreover, at 806 and 959 cm^{-1}, two bands are assigned as the symmetric vibration of Si−O−Si and Si−OH (or $Si-O^-$) stretching vibration bonds,[30] respectively. The AAS results reveal that the silica composition is 33%. The ^{29}Si CP/MAS NMR analysis in Figure 2b reveals the chemical nature of Si species in the SiO_2-TNT sample. The Q^3 species of single silanol groups $[(SiO)_3Si(OH)]$ appear in a higher proportion (56%), followed by siloxane $[(SiO)_4Si]$ (32%) and Q^2 germinal silanol groups $[(SiO)_2Si(OH)_2]$ (12%).

The porosity of SiO_2-TNT and Na-TNT samples were analyzed by N_2 adsorption/desorption isotherms shown in Figure 3a. Both isotherms exhibited the type IV profile with H3 hysteresis, typical of slit-like pore structure and characteristic of mesoporous materials, according to the IUPAC.[31] Moreover, both isotherms exhibited a steep increase in adsorption at $p/p^0 > 0.6$, which indicates interparticle mesopores. On the other hand, the higher N_2 adsorption at $p/p^0 < 0.4$ in SiO_2-TNT isotherm reveals a strong adsorbent−adsorbate interaction in the case of SiO_2-TNT resulting from its more open structure than the Na-TNT initial nanotubes. In addition, the gradient adsorption in the p/p^0 region of 0.12−0.4 in SiO_2-TNT isotherm indicates the formation of a new mesoporous structure, which is similar to other layered-type mesoporous materials (e.g., PCHs and pillared zeolites).[32−34]

Data reported in Table 1 reveals that the SiO_2-TNT material exhibits higher Brunauer−Emmett−Teller specfiic surface area (S_{BET}), microporous volume (V_{micro}), and maxcroporous volume V_{total} values than those of the Na-TNT sample. The SiO_2-TNT material exhibits a S_{BET} value of 714 $m^2\ g^{-1}$, which is greater than that of Na-TNT (58 $m^2\ g^{-1}$). Moreover, the SiO_2-TNT exhibited a V_{micro} value of 0.06 $cm^3\ g^{-1}$ suggesting that the micropores originated from the irregularity of the voids created around the silica particles and the titanate sheets.

Table 1. Textural Properties of Na-TNT and SiO_2-TNT Samples

	specific surface area		pore volume		
sample	S_{BET} ($m^2\ g^{-1}$)	S_{ext} ($m^2\ g^{-1}$)	V_{micro} ($cm^3\ g^{-1}$)	V_{total} ($cm^3\ g^{-1}$)	SiO_2 (%)[a]
Na-TNT	58	57	0	0.205	−
SiO_2-TNT	714	560	0.06	0.682	33

[a]Based in the AAS results.

The PSD of the SiO_2-TNT and Na-TNT are shown in Figures 3b and 3c, respectively. The maxima pore widths of the SiO_2-TNT material are evidenced in the regions between supermicropores and small mesopores (1.3−3.6 nm). That porosity resulted from the spacing between the titanate sheets and the silica particles in a 3D disordered orientation. On the other hand, Na-TNT exhibited mesopores with large width (>4 nm) assigned to interparticle regions between neighboring nanotubes.

TEM analyzes were performed to observe the morphological changes. Figure 4a shows elongated particles of tubular morphology, typical of titanate nanotubes. Figure 4b reveals that the nanotubes have external and internal diameters of 9.0

https://doi.org/10.1021/acs.cgd.2c01471
Cryst. Growth Des. 2023, 23, 1925−1934

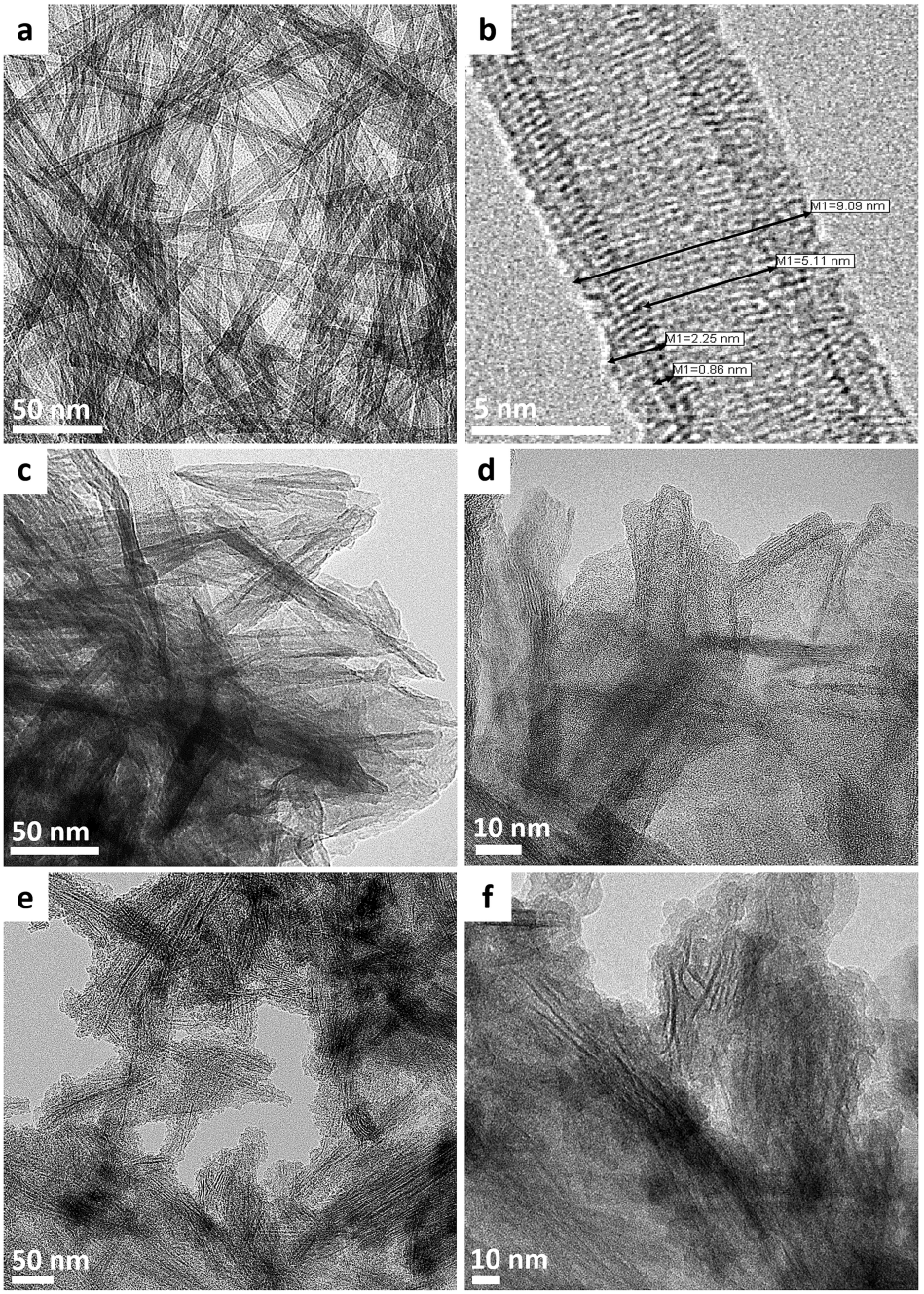

Figure 4. TEM images of (a, b) Na-TNT, (c, d) CTA-TNT, and (e, f) SiO_2-TNT samples.

and 5.1 nm, respectively. In addition, the nanotubes exhibit multiple walls measuring 2.2 nm in width, corresponding to rolled titanate sheets. The CTA-TNT sample (Figures 4c and 4d) showed larger particles, when compared to the starting nanotubes, indicating the unwinding of the nanotubes and the formation of extended nanosheets, as a result of the surfactant intercalation. The SiO_2-TNT material (Figures 4d and 4e) appear as darker and finer particles in the figure, indicating that they are far from each other in random stacking and shows that the pillaring procedure resulted in a disorganization of the titanate nanosheets. In addition, less dense particles are observed between and around the titanate nanosheets, indicating that amorphous silica was formed.

Based on the characterization results, Figure 5 summarizes the SiO_2-TNT material after treatment of the Na-TNT nanotubes with CTA molecules and the pillaring agent.

The band gap (E_g) values of Na-TNT and SiO_2-TNT were calculated by applying the Tauc relation,[35] where the linear portions of the curves are extrapolated to the x-axis ($y = 0$) to determine bandgap values (see Figure 6). The band gaps estimated for Na-TNT and SiO_2-TNT are 4.06 and 3.81 eV, respectively. The lower SiO_2-TNT band gap, compared to Na-TNT, can be attributed to the doping effect of SiO_2 present in the TNTs. Doping causes a reduction in the E_g value due to the introduction of a new electronic level, which forms the lowest unoccupied molecular orbital (LUMO) within the band-gap states of TiO_2.[36]

https://doi.org/10.1021/acs.cgd.2c01471
Cryst. Growth Des. 2023, 23, 1925−1934

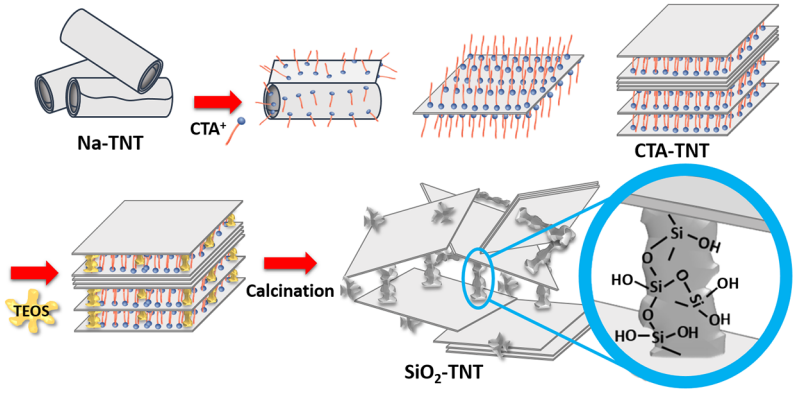

Figure 5. Representative scheme of the Na-TNT, CTA-TNT, and SiO_2-TNT materials according to the applied processes and the analysis of the solids.

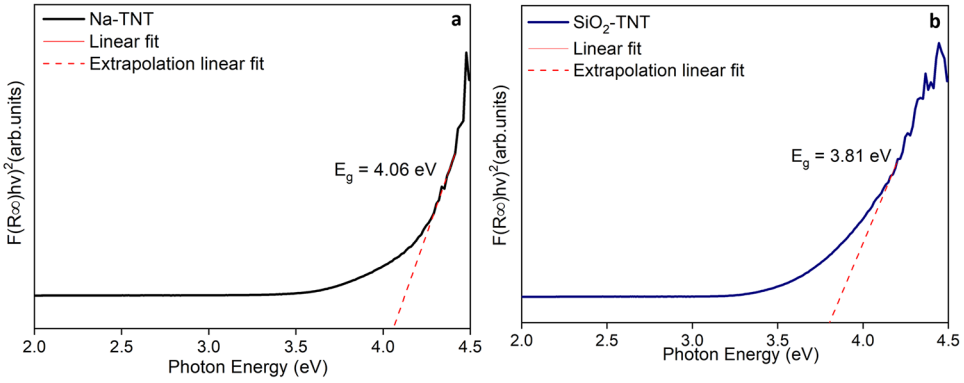

Figure 6. Tauc plots and band-gap value of (a) Na-TNT and (b) SiO_2-TNT.

The adsorptive properties of the SiO_2-TNT and Na-TNT samples were evaluated with representative cationic dyes, MB and RhB, at pH 7. The effects of concentration (q_t) and removal (%) versus contact time on MB uptake onto Na-TNT and SiO_2-TNT are depicted in Figure 7a. The q_t parameter quickly reaches equilibrium, indicating that MB molecules are in contact with surface adsorption sites available from Na-TNT and SiO_2-TNT samples, resulting in a removal efficiency of 95% and 97% for Na-TNT and SiO_2-TNT samples, respectively. The high MB adsorption by Na-TNT materials has already been widely reported in the literature.[37−40] The similar adsorption results for MB led us to investigate the performance of the Na-TNT and SiO_2-TNT samples against the other basic dye, RhB.

Figure 7b shows the q_t value and the percent removal (%R) versus time for the RhB dye. The q_t values for the Na-TNT particles indicated gradual adsorption that can be attributed to the uptake of RhB molecules into the pores of this adsorbent. The equilibrium was attained at 50 min with 13% of RhB removal. Conversely, for the SiO_2-TNT particles, the quantity of RhB dye adsorbed was observed to increase as the time and concentration each increased (65%). RhB uptake was initially rapid and reached equilibrium at 30 min. This rapid adsorption may be attributed to contacts of RhB molecules with more available surface adsorption sites of the SiO_2-TNT particles.

The different adsorption behavior observed for the cationic dyes could be explained by the positive charge of the MB molecule due to a quaternary ammonium cation (NR_4^+) in its molecule. It is also likely that both the Na-TNT and the SiO_2-TNT samples have a negative charge in MB solution at pH 7.

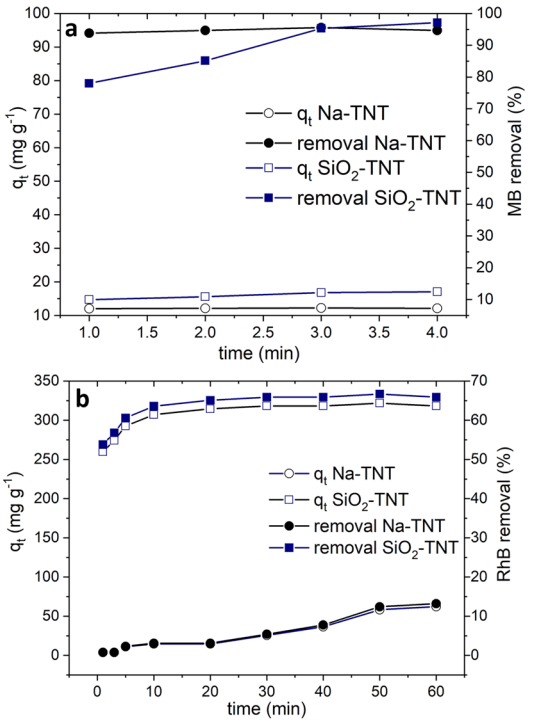

Figure 7. Time variation study for (a) MB and (b) RhB adsorption by Na-TNT and SiO_2-TNT samples.

https://doi.org/10.1021/acs.cgd.2c01471
Cryst. Growth Des. 2023, 23, 1925−1934

Thus, the attractive forces between adsorbent surface and MB molecules favored adsorption. Equally, RhB molecules have a positive charge from a quaternary ammonium cation (NR_4^+) and contain a carboxylic acid group (−COOH) and could therefore have a positive or negative surface charge, depending on the pH of the solution.[40] At pH 7, the RhB solution and the Na-TNT sample have probably the same charge, so the electrostatic repulsion between RhB molecules and the Na-TNT surface was present, leading to a decrease in adsorption. The RhB solution and the SiO_2-TNT sample likely have the same charge. However, the high RhB adsorption by the SiO_2-TNT sample can be explained by two factors: (i) the formation of hydroxyl groups on the SiO_2-TNT surface, as observed by ^{29}Si NMR, which can provide a strong electrostatic attraction for cationic dyes and (ii) the high BET surface area (714 m^2 g^{-1}) in comparison with the Na-TNT sample (58 m^2 g^{-1}).

Kinetic study models reveal the dynamic process and the mechanism of the adsorption process. Pseudo-first-order[41] and pseudo-second-order[42] kinetic models were used to study the mechanism of RhB dye adsorption onto SiO_2-TNT particles (see Figure 8). Equations 3 and 4 imply pseudo-first-order and pseudo-second-order models and are expressed as follows:

$$\ln(q_e - q_t) = \ln q_e - k_1 t \tag{3}$$

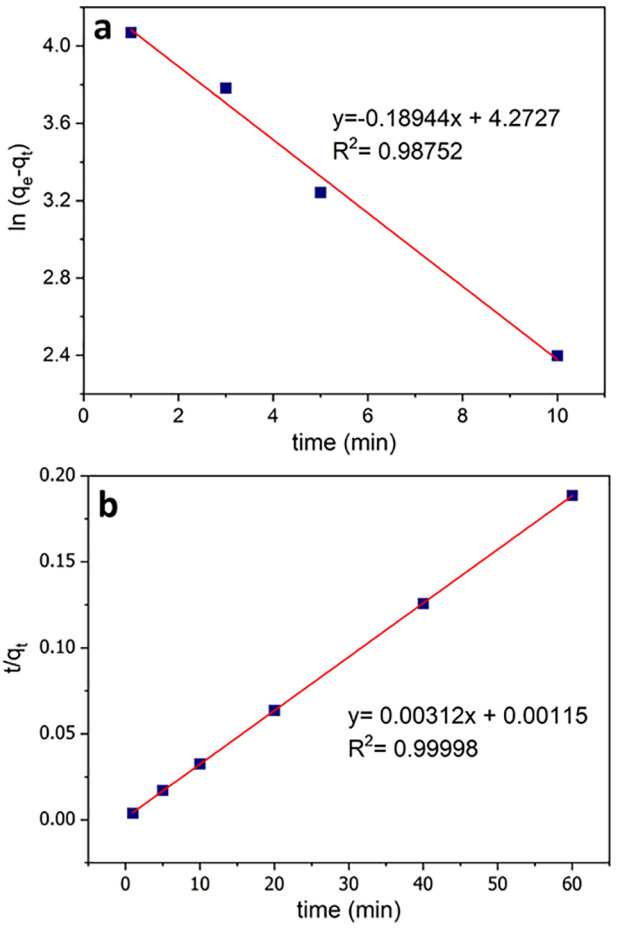

Figure 8. (a) Pseudo-first-order kinetics and (b) pseudo-second-order kinetics for RhB dye adsorption onto SiO_2-TNT at various initial concentrations.

$$\frac{t}{q_t} = \frac{1}{k_2 q_e^{\,2}} + \frac{t}{q_e} \tag{4}$$

where q_e and q_t are the absorbed amounts onto SiO_2-TNT at equilibrium and at time t (min), respectively (eq 3). k_1 and k_2 (min^{-1}) are the rates constant of the pseudo-first-order and pseudo-second-order equations, and t is the contact time of the adsorption process (eq 4).

Through the plots of $\ln(q_e - q_t)$ vs t (Figure 8a) and t/q_t vs t (Figure 8b), the values of the parameters k_1, k_2, q_e, and R^2 were obtained, and the calculated values are shown in Table 2.

The results show that the pseudo-second-order model fits the experimental data better, since the q_e calculated values are closer to the experimental results (q_e, experimental), and the R^2 value obtained from the pseudo-second-order model (R^2 - 0.9999) was higher than that calculated from the pseudo-first-order model.

The adsorption isotherm is a model to explore how the adsorbed ions are distributed over the adsorbent. The experimental results were fitted to the two most used isotherm models: Langmuir[43] and Freundlich.[44] The Langmuir adsorption isotherm and the linear form of Freundlich isotherm are expressed by eqs 5 and 6:

$$\frac{C_e}{q_e} = \frac{1}{q_m k_L} + \frac{C_e}{q_m} \tag{5}$$

$$\ln q_e = \ln k_f + \frac{1}{n \ln C_f} \tag{6}$$

where C_e is the concentration (mg L^{-1}) of RhB dye solution at equilibrium, q_e the equilibrium amount of dye adsorbed (mg g^{-1}), q_m the maximum capacity of adsorption (mg g^{-1}), and K_L the Langmuir constant related to adsorption energy. K_L and q_m values can be obtained from the intercept and slope of the linear plot of C_e/q_e vs C_e (Figure 9b). In the Freundlich equation, the parameters K_f and $1/n$ are Freundlich constants, representing the adsorption capacity and intensity of adsorption, respectively.[45] Through a linear plot of ln q_e vs ln C_f (Figure 9c), the values of $1/n$ and K_f can be obtained from the slope and intercept, respectively.

Results reported in Table 3 show that the Freundlich model best fits the adsorption data indicated by the higher R^2 value (0.90994), compared to the Langmuir isotherm model (R^2 = 0.11071). The high R^2 value suggests that adsorption was not onto uniform sites, but multilayer adsorption occurred onto RhB/SiO_2-TNT material. The Freundlich constant ($1/n$) is associated with the sorbent's sorption intensity. When $0.1 < 1/n \leq 0.5$, adsorption is extremely easy; at $0.5 < 1/n \leq 1$, adsorption is easy; and at $1/n > 1$, adsorption is difficult.[46] The $1/n$ value obtained was 0.84, indicating that RhB could easily be adsorbed onto SiO_2-TNT particles.

4. CONCLUSION

This work has demonstrated that it is possible to obtain silica−titanate nanoarchitectures with a high surface area by unwinding tubular titanates aided by positively charged long-chain surfactants. The characterization techniques showed that the organic−inorganic hybrid intermediate presented lamellar stacking order, resulting from the perpendicular accommodation of the surfactant molecules between the titanate lamellae. The introduction of the pillaring agent caused the loss of the lamellar stacking order, resulting in a delaminated structure

https://doi.org/10.1021/acs.cgd.2c01471
Cryst. Growth Des. 2023, 23, 1925−1934

Table 2. Kinetic Model Parameters for RhB Adsorption over the SiO_2-TNT Sample

	pseudo-first-order			pseudo-second-order		
q_e (experimental)	k_1 (min^{-1})	q_e (mg/g)	R^2	k_2 (g/mg min)	q_e (mg/g)	R^2
318.2	0.18944	71.71	0.9875	0.00846	320.5	0.9999

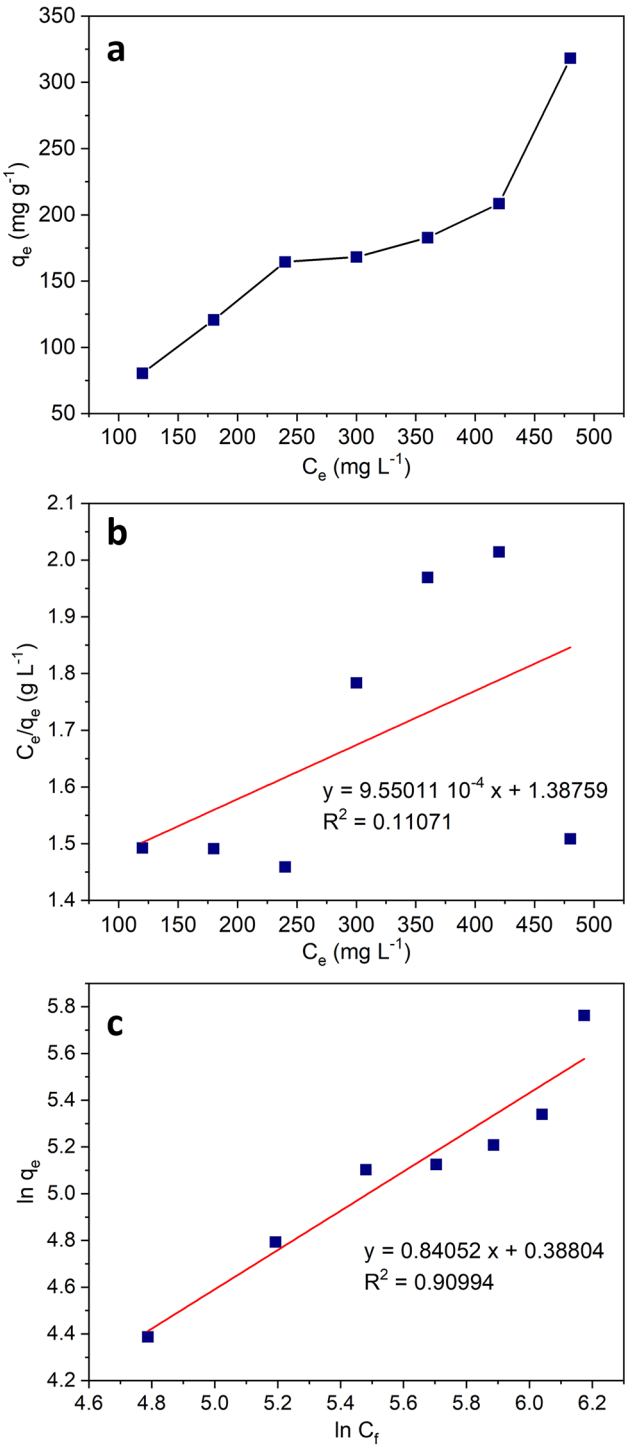

Figure 9. (a) Effect of initial RhB concentration on the adsorption capacity (SiO_2-TNT dose = 50 mg, RhB concentration = 120−480 mg L^{-1}); (b) Langmuir isotherm and (c) Freundlich isotherm for RhB adsorption over the SiO_2-TNT sample.

composed of titanate lamellae spaced by silica particles and combined regions of micropores and mesopores able to adsorb

Table 3. Adsorption Isotherm Parameters for RhB Adsorption by the SiO_2-TNT Sample

Langmuir			Freundlich		
q_m (mg g^{-1})	k_L (L mg^{-1})	R^2	k_F (mg g^{-1})	n	R^2
1047.1	6.88×10^{-4}	0.11071	1.4741	1.189	0.90994

voluminous molecules such as MB and RhB organic dyes. In the case of the RhB dye, the SiO_2-TNT material has a higher adsorption ability than Na-TNT associated to its more-open pore structure. The data have demonstrated that SiO_2-TNT nanocomposites have the potential to serve as a dye adsorbent to treat effluents, especially those containing cationic dyes.

AUTHOR INFORMATION

Corresponding Authors

Anderson J. Schwanke − *Instituto de Química, Universidade Federal do Rio Grande do Sul (UFRGS), 91501-970 Porto Alegre, RS, Brasil;* orcid.org/0000-0002-1273-9940; Email: anderson.schwanke@ufrgs.br

Michèle O. de Souza − *Instituto de Química, Universidade Federal do Rio Grande do Sul (UFRGS), 91501-970 Porto Alegre, RS, Brasil;* orcid.org/0000-0001-8039-3753; Email: michele.souza@ufrgs.br

Authors

Wesley Monteiro − *Instituto de Química, Universidade Federal do Rio Grande do Sul (UFRGS), 91501-970 Porto Alegre, RS, Brasil; Programa de Pós-Graduação em Engenharia e Tecnologia de Materiais, Pontifícia Universidade Católica do Rio Grande do Sul (PUCRS), 90619-900 Porto Alegre, RS, Brasil*

Letícia G. da Trindade − *Departamento de Engenharia Química, Universidade Federal de São Paulo (UNIFESP), 09972-270 Diadema, SP, Brasil*

Elson Longo − *Universidade Federal de São Carlos (UFSCar), Departamento de Química, 13560-970 São Carlos, SP, Brasil*

Katia Bernardo-Gusmão − *Instituto de Química, Universidade Federal do Rio Grande do Sul (UFRGS), 91501-970 Porto Alegre, RS, Brasil;* orcid.org/0000-0003-3115-6844

Complete contact information is available at: https://pubs.acs.org/10.1021/acs.cgd.2c01471

Notes

The authors declare no competing financial interest.

ACKNOWLEDGMENTS

The authors thank the FAPERGS and SICT (INOVACLEAN Project) and MCTI/FINEP (REJEMEA and MULTIMAT Projects).

https://doi.org/10.1021/acs.cgd.2c01471
Cryst. Growth Des. 2023, 23, 1925−1934

REFERENCES

(1) Shen, S.; Chen, J.; Wang, M.; Sheng, X.; Chen, X.; Feng, X.; Mao, S. S. Titanium dioxide nanostructures for photoelectrochemical applications. *Prog. Mater. Sci.* **2018**, *98*, 299−385.

(2) Zhang, W.; Tian, Y.; He, H.; Xu, L.; Li, W.; Zhao, D. Recent advances in the synthesis of hierarchically mesoporous TiO_2 materials for energy and environmental applications. *Natl. Sci.* **2020**, *7* (11), 1702−1725.

(3) Zhang, Y.; Jiang, Z.; Huang, J.; Lim, L. Y.; Li, W.; Deng, J.; Gong, D.; Tang, Y.; Lai, Y.; Chen, Z. Titanate and titania nanostructured materials for environmental and energy applications: A review. *RSC Adv.* **2015**, *5* (97), 79479−79510.

(4) Kordás, K.; Mohl, M.; Kónya, Z.; Kukovecz, A. Layered titanate nanostructures: perspectives for industrial exploitation. *Trans. Mater. Res.* **2015**, *2* (1), 015003.

(5) Izawa, H.; Kikkawa, S.; Koizumi, M. Ion exchange and dehydration of layered [sodium and potassium] titanates, $Na_2Ti_3O_7$ and $K_2Ti_4O_9$. *J. Phys. Chem.* **1982**, *86* (25), 5023−5026.

(6) Sasaki, T.; Komatsu, Y.; Fujiki, Y. Protonated pentatitanate: preparation, characterizations and cation intercalation. *Chem. Mater.* **1992**, *4* (4), 894−899.

(7) Kooli, F.; Sasaki, T.; Mizukami, F.; Watanabe, M.; Martin, C.; Rives, V. Characterization and acidic properties of silica pillared titanates. *J. Mater. Chem.* **2001**, *11* (3), 841−845.

(8) Kooli, F.; Sasaki, T.; Rives, V.; Watanabe, M. Synthesis and characterization of a new mesoporous alumina-pillared titanate with a double-layer arrangement structure. *J. Mater. Chem.* **2000**, *10* (2), 497−501.

(9) Anderson, M. W.; Klinowski, J. Layered titanate pillared with alumina. *Inorg. Chem.* **1990**, *29* (17), 3260−3263.

(10) Yanagisawa, M.; Uchida, S.; Yin, S.; Sato, T. Synthesis of Titania-Pillared Hydrogen Tetratitanate Nanocomposites and Control of Slit Width. *Chem. Mater.* **2001**, *13* (1), 174−178.

(11) Choy, J.-H.; Lee, H.-C.; Jung, H.; Hwang, S.-J. A novel synthetic route to TiO_2-pillared layered titanate with enhanced photocatalytic activity. *J. Mater. Chem.* **2001**, *11* (9), 2232−2234.

(12) Tsiamtsouri, M. A.; Allan, P. K.; Pell, A. J.; Stratford, J. M.; Kim, G.; Kerber, R. N.; Magusin, P. C. M. M.; Jefferson, D. A.; Grey, C. P. Exfoliation of Layered Na-Ion Anode Material $Na_2Ti_3O_7$ for Enhanced Capacity and Cyclability. *Chem. Mater.* **2018**, *30* (5), 1505−1516.

(13) Kasuga, T.; Hiramatsu, M.; Hoson, A.; Sekino, T.; Niihara, K. Formation of Titanium Oxide Nanotube. *Langmuir* **1998**, *14* (12), 3160−3163.

(14) Bavykin, D. V.; Parmon, V. N.; Lapkin, A. A.; Walsh, F. C. The effect of hydrothermal conditions on the mesoporous structure of TiO_2 nanotubes. *J. Mater. Chem.* **2004**, *14* (22), 3370−3377.

(15) Lee, C.-K.; Lin, K.-S.; Wu, C.-F.; Lyu, M.-D.; Lo, C.-C. Effects of synthesis temperature on the microstructures and basic dyes adsorption of titanate nanotubes. *J. Hazard. Mater.* **2008**, *150* (3), 494−503.

(16) Du, A. J.; Sun, D. D.; Leckie, J. O. Sequestration of cadmium ions using titanate nanotube. *J. Hazard. Mater.* **2011**, *187* (1), 401−406.

(17) Kitano, M.; Wada, E.; Nakajima, K.; Hayashi, S.; Miyazaki, S.; Kobayashi, H.; Hara, M. Protonated Titanate Nanotubes with Lewis and Brønsted Acidity: Relationship between Nanotube Structure and Catalytic Activity. *Chem. Mater.* **2013**, *25* (3), 385−393.

(18) Pan, H.; Wang, W.; Pan, Y.; Song, L.; Hu, Y.; Liew, K. M. Formation of Layer-by-Layer Assembled Titanate Nanotubes Filled Coating on Flexible Polyurethane Foam with Improved Flame Retardant and Smoke Suppression Properties. *ACS Appl. Mater. Interfaces.* **2015**, *7* (1), 101−111.

(19) Hong, Z.; Wei, M. Layered titanate nanostructures and their derivatives as negative electrode materials for lithium-ion batteries. *J. Mater. Chem. A* **2013**, *1* (14), 4403−4414.

(20) Joshi, B.; Regmi, C.; Dhakal, D.; Gyawali, G.; Lee, S. W. Efficient inactivation of Staphylococcus aureus by silver and copper loaded photocatalytic titanate nanotubes. *Prog. Nat. Sci.* **2018**, *28* (1), 15−23.

(21) Alban, L.; Monteiro, W. F.; Diz, F. M.; Miranda, G. M.; Scheid, C. M.; Zotti, E. R.; Morrone, F. B.; Ligabue, R. New quercetin-coated titanate nanotubes and their radiosensitization effect on human bladder cancer. *Mater. Sci. Eng., C* **2020**, *110*, 110662.

(22) Gao, T.; Wu, Q.; Fjellvåg, H.; Norby, P. Topological Properties of Titanate Nanotubes. *J. Phys. Chem. C* **2008**, *112* (23), 8548−8552.

(23) Monteiro, W. F.; dos Santos, C. A. B.; Einloft, S.; Oberson, M.; Carone, C. L. P.; Ligabue, R. A. Preparation of Modified Titanate Nanotubes and Its Application in Polyurethane Nanocomposites. *MacMacromol. Symp.* **2016**, *368* (1), 93−97.

(24) Olivier, J. P.; Occelli, M. L. Surface Area and Microporosity of a Pillared Interlayered Clay (PILC) from a Hybrid Density Functional Theory (DFT) Method. *J. Phys. Chem. B* **2001**, *105* (3), 623−629.

(25) Sales, D. A.; Marques, T. M. F.; Ghosh, A.; Gusmão, S. B. S.; Vasconcelos, T. L.; Luz-Lima, C.; Ferreira, O. P.; Hollanda, L. M.; Lima, I. S.; Silva-Filho, E. C.; Dittz, D.; Lobo, A. O.; Viana, B. C. Synthesis of silver−cerium titanate nanotubes and their surface properties and antibacterial applications. *Mater. Sci. Eng., C* **2020**, *115*, 111051.

(26) Hlawacek, G.; Ahmad, I.; Smithers, M. A.; Kooij, E. S. To see or not to see: Imaging surfactant coated nano-particles using HIM and SEM. *Ultramicroscopy* **2013**, *135*, 89−94.

(27) Monteiro, W. F.; Vieira, M. O.; Laschuk, E. F.; Livotto, P. R.; Einloft, S. M. O.; de Souza, M. O.; Ligabue, R. A. Experimental-theoretical study of the epoxide structures effect on the CO2 conversion to cyclic carbonates catalyzed by hybrid titanate nanostructures. *J. CO2 Util.* **2020**, *37*, 20−28.

(28) Monteiro, W. F.; dos Santos, C. A. B.; Hoffmann, M. S.; Carone, C. L. P.; Einloft, S. M. O.; de Souza, M. O.; Ligabue, R. A. Modified titanate nanotubes for the production of novel aliphatic polyurethane nanocomposites. *Polym. Compos.* **2019**, *40* (6), 2292−2300.

(29) Venkataraman, N. V.; Vasudevan, S. Conformation of Methylene Chains in an Intercalated Surfactant Bilayer. *J. Phys. Chem. B* **2001**, *105* (9), 1805−1812.

(30) Warring, S. L.; Beattie, D. A.; McQuillan, A. J. Surficial Siloxane-to-Silanol Interconversion during Room-Temperature Hydration/Dehydration of Amorphous Silica Films Observed by ATR-IR and TIR-Raman Spectroscopy. *Langmuir* **2016**, *32* (6), 1568−1576.

(31) Thommes, M.; Kaneko, K.; Neimark, A. V.; Olivier, J. P.; Rodriguez-Reinoso, F.; Rouquerol, J.; Sing, K. S. W. Physisorption of gases, with special reference to the evaluation of surface area and pore size distribution (IUPAC Technical Report). *Pure Appl. Chem.* **2015**, *87*, 1051.

(32) Sato, K.; Fujikawa, E.; Cecilia, J. A. Increased Protonation of a Mesopore Surface in a Porous Clay Nanoheterostructure. *J. Phys. Chem. C* **2022**, *126* (30), 12615−12622.

(33) Hao, Q.-Q.; Liu, Z.-W.; Zhang, B.; Wang, G.-W.; Ma, C.; Frandsen, W.; Li, J.; Liu, Z.-T.; Hao, Z.; Su, D. S. Porous Montmorillonite Heterostructures Directed by a Single Alkyl Ammonium Template for Controlling the Product Distribution of Fischer−Tropsch Synthesis over Cobalt. *Chem. Mater.* **2012**, *24* (6), 972−974.

(34) Zukal, A.; Kubů, M. High-resolution adsorption analysis of pillared zeolites IPC-3PI and MCM-36. *Dalton Trans.* **2014**, *43* (27), 10558−10565.

(35) Alam, N.; Khatoon, T.; Chandel, V. S.; Azam, A. Band Gap Engineering in Zinc Doped Sodium Hexa-titanate. *Indian J. Sci. Technol.* **2019**, *12* (21), 5.

(36) Devi, L. G.; Kottam, N.; Murthy, B. N.; Kumar, S. G. Enhanced photocatalytic activity of transition metal ions Mn^{2+}, Ni^{2+} and Zn^{2+} doped polycrystalline titania for the degradation of Aniline Blue under UV/solar light. *J. Mol. Catal. A: Chem.* **2010**, *328* (1), 44−52.

(37) Sandoval, A.; Hernández-Ventura, C.; Klimova, T. E. Titanate nanotubes for removal of methylene blue dye by combined adsorption and photocatalysis. *Fuel* **2017**, *198*, 22−30.

https://doi.org/10.1021/acs.cgd.2c01471
Cryst. Growth Des. 2023, 23, 1925−1934

(38) Wang, Q.; Lei, X.; Pan, F.; Xia, D.; Shang, Y.; Sun, W.; Liu, W. A new type of activated carbon fibre supported titanate nanotubes for high-capacity adsorption and degradation of methylene blue. *Colloids Surf. A: Physicochem. Eng. Asp.* **2018**, *555*, 605−614.
(39) Baiju, K. V.; Shukla, S.; Biju, S.; Reddy, M. L. P.; Warrier, K. G. K. Hydrothermal processing of dye-adsorbing one-dimensional hydrogen titanate. *Mater. Lett.* **2009**, *63* (11), 923−926.
(40) Hsieh, C.-T.; Fan, W.-S.; Chen, W.-Y. Impact of mesoporous pore distribution on adsorption of methylene blue onto titania nanotubes in aqueous solution. *Microporous Mesoporous Mater.* **2008**, *116* (1), 677−683.
(41) Lagergren S, K. About the Theory of So-called Adsorption of Soluble Substances. *Sven. Vetenskapsakad. Handingarl* **1898**, *24*, 1−39.
(42) Ho, Y. S.; McKay, G. Pseudo-second order model for sorption processes. *Process Biochem.* **1999**, *34* (5), 451−465.
(43) Langmuir, I. The adsorption of gases on plane surfaces of glass, mica and platinum. *J. Am. Chem. Soc.* **1918**, *40* (9), 1361−1403.
(44) Umpleby, R. J.; Baxter, S. C.; Bode, M.; Berch, J. K.; Shah, R. N.; Shimizu, K. D. Application of the Freundlich adsorption isotherm in the characterization of molecularly imprinted polymers. *Anal. Chim. Acta* **2001**, *435* (1), 35−42.
(45) Halsey, G. D. The Role of Surface Heterogeneity in Adsorption. *Adv. Catal.* **1952**, *4*, 259−269.
(46) Tang, H.; Zhou, W.; Zhang, L. Adsorption isotherms and kinetics studies of malachite green on chitin hydrogels. *J. Hazard. Mater.* **2012**, *209*−*210*, 218−225.

https://doi.org/10.1021/acs.cgd.2c01471
Cryst. Growth Des. 2023, 23, 1925−1934